ROYAL SOCIETY
OF CHEMISTRY

Check for updates

Microwave-assisted carbon-confined iron nanoparticles for steering CO₂ hydrogenation to heavy hydrocarbons†

Lisheng Guo, [ID] *[ab] Peipei Ai,[b] Xinhua Gao, [ID] [c] Hao Wu,[a] Xianbiao Wang,[a] Yasuharu Kugue,[d] Jiaming Liang,[d] Weizhe Gao,[d] Xiaoyu Guo,[d] Jian Sun, [ID] *[e] Song Sun [ID] *[a] and Noritatsu Tsubaki [ID] *[d]

The key to efficient thermocatalytic conversion of CO₂ lies in the rational design of catalysts. In this work, Fe-based catalysts supported by different carbon materials (AC, GA, CNF, and MPC) were rapidly synthesized with the assistance of microwave heating. Compared with other supports, small-sized active precursors are coated by graphitic carbon layers for GA-supported Fe catalysts, which will slow down the sintering of particles. Small-sized Fe nanoparticles supported by GA present a benign carburization behavior and water removal ability, which play an important role in stabilizing active carbides and improving product selectivity. These features make GA a more promising support material. In addition, for the catalyst obtained by high-temperature calcination, the size of the active precursor is larger than that obtained by microwave heating, and it is easily coated by amorphous carbon shells, whereas for the small active phase precursor obtained by microwave heating treatment, it is encapsulated by graphitic carbons first, and then the amorphous carbon shells gradually appear around the active carbides with the increase in particle size. The carbon-confined environment provides a stable space for steering CO₂ hydrogenation to heavy hydrocarbons. As a result, the rational catalyst exhibits favorable performance. Under relevant industrial conditions (320 °C, 2.0 MPa, 5 g h mol⁻¹), the optimized K–Fe/GA-W-10 catalyst achieves a C₅₊ selectivity of 53.2% at CO₂ conversion of 23.1% and presents a benign stability.

Broader context

The transformation of CO₂ into energy-rich fuels and valuable chemicals is a huge challenging and hot research topic. The critical bottleneck of this process lies in the difficult activation of inert CO₂ molecules and poor chain growth ability. Efficient catalyst preparation is one of the key strategies to solve this problem and for potential industrial applications. At present, conventional catalyst synthesis requires high-temperature calcination to obtain the precursor, which usually consumes a good chunk of time. In addition, high-temperature calcination will also destroy the special structure of the catalyst. To overcome this huge challenge, we designed microwave-assisted carbon-confined iron nanoparticle catalysts for steering CO₂ hydrogenation to heavy hydrocarbons. The high-temperature treatment lasts only a few seconds, and this method promotes the formation of ultra-high dispersion active metal sites. Moreover, the carbon-confined structure is conducive to CO₂ conversion, and maintains the active phase stably. Consequently, the tailor-made catalyst presents benign performance. The present research provides new insights for the rapid fabrication of high-performance catalysts for practical industrial applications in catalytic conversions of C1 small molecules to high value-added chemicals. More importantly, the unique encapsulation and uniform dispersion of active sites from the microwave heating technology have good reference significance for other supported catalysts.

a School of Chemistry and Chemical Engineering, Anhui University, Hefei, Anhui 230601, China. E-mail: lsguo@ahu.edu.cn, suns@ustc.edu.cn

b State Key Laboratory of Clean and Efficient Coal Utilization, Taiyuan University of Technology, Taiyuan 030024, Shanxi, China

c State Key Laboratory of High-efficiency Utilization of Coal and Green Chemical Engineering, College of Chemistry & Chemical Engineering, Ningxia University, Yinchuan 750021, China

d Department of Applied Chemistry, School of Engineering, University of Toyama, Gofuku 3190, Toyama 930-8555, Japan. E-mail: tsubaki@eng.u-toyama.ac.jp

e Dalian Institute of Chemical Physics, Chinese Academy of Sciences, Dalian 116023, China. E-mail: sunj@dicp.ac.cn

† Electronic supplementary information (ESI) available. See DOI: https://doi.org/10.1039/d3ey00071k

Introduction

Almost a century on, massive CO₂ emissions result in several environmental issues related to global warming, ocean acidification, *etc.*, whereas thermocatalytic CO₂ hydrogenation provides a promising route for CO₂ elimination and reutilization.[1–6] Selective hydrogenation of CO₂-derived highly valuable products including carbon monoxide (CO), alcohols, alkenes, aromatics, oxygenates, and liquid hydrocarbons is necessary.[7–11] Among them, liquid or long-chain hydrocarbons, as substitutable fuels, are one of the most desirable products.[10,12–15]

Recently, significant advances in the selective synthesis of liquid hydrocarbons from CO_2 hydrogenation have been reported by constructing efficient functional catalysts.[10,12,13] Yet, it remains a huge challenge to directly convert CO_2 into liquid hydrocarbons, since CO_2 molecules are thermodynamically stable and carbon chain propagation needs to overcome higher energy barriers. In terms of CO_2 hydrogenation, raw molecules can be catalyzed to valuable products over modified metal oxides or multi-site composite functional catalysts.[16–18]

Iron as a typical catalyst can *in situ* form two types of active sites under CO_2/H_2 conditions, including Fe_3O_4 for reverse water–gas shift (RWGS) and carbides (Fe_xC_y) for chain growth, and they have been widely applied for CO_2 hydrogenation *via* modified Fischer–Tropsch synthesis (FTS). Generally, a single iron catalyst without any regulation presents a poor catalytic performance such as low catalytic activity and high light hydrocarbon selectivity, far from needs and expectations. To address this issue, a series of tailor-made iron-based catalysts were synthesized by regulating CO_x adsorption, electronic environments of active sites, interaction between active metal and support materials, *etc.* A common means is to introduce electronic promoters in the iron-based system, usually referring to alkali metals (Li, Na, and K), alkaline-earth metals (Mg, Ca, and Sr), and transition metals (Cu, Mn, Zn, Zr, Mo, V, and Nb). Given the excellent promotional effects, K and Na promoters are widely selected for modifying iron-based catalysts to achieve benign catalytic performance. The existence of Na or K above can enhance the surface alkalinity, promoting the adsorption of CO_x molecules.[19] With the incorporation of promoters such as Na, delocalized electrons are transferred from the electronic promoter to the interface of iron carbides, making the surface of iron carbides electron rich.[20] CO activation on carbides occurs *via* Fe–C σ-bonding and the simultaneous back-donation of iron species valence electrons into the $2\pi^*$ orbital of CO.[21] The enhanced electron density of carbides derived from electron transfer is able to intensify the Fe–C bond and weakens the C–O bond.[22] Besides, more carbides are formed with the introduction of alkali metals.[23,24] Unlike the Na promoter, it is accepted that K is more suitable for the formation of long-chain hydrocarbons.[19,24–27]

Apart from the promoter modification, controlling the interaction between the active metal and the support is adopted as another important means.[28,29] Conventional oxide supports such as Al_2O_3, SiO_2, and TiO_2 have been widely used in Fe-based catalysts for CO_2 conversion. However, a strong interaction between Fe and the oxide support may form a hardly reducible iron species (for example, iron silicates) and inhibit the reduction and carburization of an active Fe phase during the CO_2 hydrogenation. Furthermore, various types of carbonaceous supports such as carbon nanofibers (CNFs), mesoporous carbons (MPCs), activated carbons (ACs), and graphenes (GAs) have been regarded as promising catalytic supports due to their tunable surface properties, thermal stability, and weak metal–support interactions.[22,30–33] Although some advances have been reported, carbonaceous materials as promising supports have not yet received enough attention in the process of CO_2 hydrogenation

to long-chain hydrocarbons, let along the differences of promotional effects among different carbonaceous supports. Previously, we have designed supported iron nanoparticles for FTS by utilizing "microwave dielectric heating" effects, in which iron species presents benign dispersion.[34] Microwave energy, when incident on a lossy dispersive material, generates heat within the material *via* the interactions of the electromagnetic field with the material's molecular and electronic structures. According to the Poynting theorem, the total power entering a volume V through the surface S goes partially into increasing the field energy stored inside V and is partially lost into heat.[35] It can be judged that the ability of a material to heat up in the presence of an electromagnetic wave depends on the nature of its interaction with electric and magnetic components of the field. Generally, carbonaceous materials (graphite, graphenes, *etc.*) are dielectric absorbers having a sp^2 bonded carbon network, which contains copious amounts of delocalized π electrons, which in the presence of an external electric field, start moving in the direction of the field and generate an electric current. As the electrons cannot couple to the changes of phase of the electric field, energy in the form of heat is dissipated. This process is referred to as interfacial polarization (also known as the Maxwell–Wagner–Sillars effect).[36–38]

In this work, a series of carbon material (including GA, CNF, AC, and MPC)-supported iron nanoparticles were prepared for CO_2 conversion, where the precursors were treated by rapid microwave heating (MH). The improved dispersion, carburization behavior, and water removal ability are responsible to the high selectivity of long-chain hydrocarbons. Thereinto, a small-sized Fe nanoparticle encapsulated in a carbon shell is a key feature structure, which effectively stabilizes the carbide active phase and provides a favorable carbon environment. Correspondingly, a GA-supported Fe nanoparticle catalyst reaches C_{5+} selectivity as high as 53.2% at CO_2 conversion of 23.1% (Scheme 1).

Experimental

Catalyst preparation

Commercial GA, CNF, MPC, and AC were selected as carbonaceous supports. Prior to utilization, the carbon supports were filtered, washed with deionized water and then dried. Subsequently, 15 wt% Fe and 5 wt% K were introduced into the support by an incipient wetness impregnation method. It was then vacuum dried at 80 °C for 10 h to remove water. The obtained catalyst was treated with microwave for 10 seconds under the protection of N_2 atmosphere (using a 700 W microwave oven). In each experimental synthesis, 0.5 g catalyst precursor was evenly placed in a Petri dish. Then it was moved into a microwave oven and placed in the center of the oven. It is worth noting that the whole microwave oven was placed in a glove box with nitrogen gas as the protective gas (Fig. S1, ESI†). Finally, the corresponding catalysts were marked as K–Fe/GA-W-10, K–Fe/CNF-W-10, K–Fe/AC-W-10, and K–Fe/MPC-W-10, respectively.
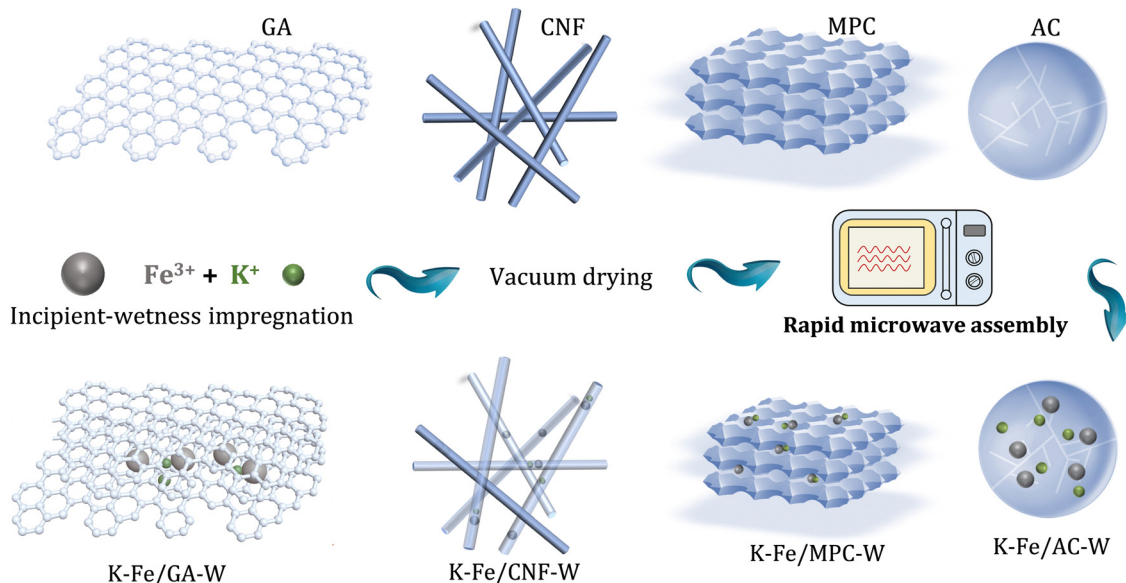
Scheme 1 Schematic diagram of the synthesis of different catalysts *via* facile microwave heating treatment.

In addition, in order to investigate the effect of microwave treatment time, the catalysts treated for different microwave time periods were prepared, marked as K–Fe/GA-W-*t* (*t* = 0, 5, and 15 s). Meanwhile, a K–Fe/GA catalyst was also fabricated *via* muffle calcination at different temperatures (*T* = 550, 700, or 850 °C for 5 h) under the protection of N_2 atmosphere and labelled as K–Fe/GA-C-T.

By contrast, a SiO_2-supported iron catalyst was also fabricated. Similar to carbon material-supported Fe catalysts, same contents of Fe and K were introduced into SiO_2 by the same method. Considering that microwave heating could not heat SiO_2, the obtained precursor was calcined in a muffle (550 °C for 5 h) under the protection of N_2 atmosphere, and the obtained catalyst was labeled as K–Fe/SiO_2-C-550.

Catalyst characterization

Ex situ powder X-ray diffraction (XRD) data were acquired using a Rigaku RINT 2400 X-ray Diffractometer with Cu Kα radiation (40 kV, 40 mA). A step size of 0.02° s^{-1} over a 2θ range of 20–80° was adopted.

In situ XRD data were conducted using an Empyrean-100 PANalytical Empyrean-100 373 diffractometer with Cu Kα irradiation. The catalyst was first exposed to a H_2 atmosphere for reduction, and the temperature was gradually increased from room temperature to 400 °C. After reduction at 400 °C for 90 min, the temperature was decreased to 320 °C. Subsequently, CO_2 and H_2 (H_2/CO_2 = 3) were introduced to the catalyst with a reaction pressure of 1.0 bar. The XRD patterns were collected over time.

N_2 adsorption–desorption curves were measured at −196 °C using a NOVA 2200e apparatus to determine the specific surface area based on the Brunauer–Emmett–Teller (BET) method. Before measurement, the catalyst was outgassed under vacuum at 200 °C for 6 h.

A BELCAT-II-T-SP analyser was used to perform the H_2-temperature programmed reduction (H_2-TPR) and CO_2-temperature programmed desorption (CO_2-TPD). For H_2-TPR, 50 mg catalyst was pretreated at 150 °C with Ar for 1 h. Subsequently, 5 vol% H_2/Ar gas mixture was fed into the reactor when the temperature dropped to 50 °C. Finally, the H_2-TPR trace was recorded from 50 to 800 °C at a heating rate of 10 °C min^{-1}. As for CO_2-TPD, 50 mg catalyst was reduced at 400 °C for 2 h in flowing 5 vol% H_2/Ar. After pretreatment, the catalyst was flushed in an Ar flow for 30 min. Then, the temperature was decreased to 50 °C in the Ar flow and saturated with CO_2 for 30 min. After flushing in the Ar flow for 30 min, CO_2-TPD signals were recorded from 50 to 800 °C at a heating rate of 10 °C min^{-1}.

X-ray photoelectron spectroscopy (XPS) analysis was performed using a Thermo Fisher Scientific ESCALAB 250Xi multifunctional X-ray photoelectron instrument.

Transmission electron microscopic (TEM) images of catalysts were acquired using a JEOL JEM-3200Fs at an accelerating voltage of 100 kV.

Raman spectroscopy measurements were taken using a HORIBA HR Evolution Raman spectrometer with a 2 mW 532 nm excitation laser. The exposure time for each line was 10 s, and the number of exposures was 2.

The static water contact angle was measured using a DSA100M (Theta Flex) in an environmental chamber saturated with water vapor under ambient conditions.

Catalyst evaluation

The CO_2 hydrogenation reaction was carried out in a fixed-bed reactor with the condition of 320 °C, 2.0 MPa and 4800 mL g$_{cat}^{-1}$ h^{-1}. The catalyst was diluted with SiO_2 (1 : 1 mass ratio of the catalyst : silica). Before the reaction, the catalyst was reduced by H_2 at 400 °C for 10 h. After reduction,

the given conditions were adopted to test the performance of CO_2 hydrogenation. Gas chromatography (GC) was used to determine the conversion and product selectivities. The light hydrocarbons (C_1–C_7) were analyzed using an online GC with a flame ionization detector (FID). The outlet gas (Ar, CO, CH_4 and CO_2) was analyzed using another GC system with a thermal conductivity detector (TCD). The heavy hydrocarbons (C_{5+}) were collected using an ice-trap and analyzed using an off-line GC with n-dodecane (0.1 g) as an internal standard. The calculation method for CO_2 conversion, CO selectivity and hydrocarbon selectivity has been previously reported in the literature.[22,39]

Results and discussions

Oriented synthesis of heavy hydrocarbons from CO_2 hydrogenation

CO_2 hydrogenation performances were investigated over different material-supported Fe nanoparticles (K–Fe/AC-W-10, K–Fe/CNF-W-10, K–Fe/GA-W-10, K–Fe/MPC-W-10, and K–Fe/SiO$_2$-C-550) with a condition of 320 °C, 2.0 MPa, 4800 mL g_{cat}^{-1} h^{-1}. The catalytic activities and product distributions are summarized in Table 1. The K–Fe/AC-W-10 catalyst exhibits 16.4% selectivity to CH_4, 44.7% selectivity to C_{5+} as well as a moderate CO selectivity (40.2%) at CO_2 conversion of 26.3%. Thereinto, unsaturated alkenes, especially long-chain hydrocarbons, are dominant in hydrocarbon products due to the promotional effect of the alkaline K promoter (Fig. S2, ESI†).[24] Meanwhile, C_{5+} hydrocarbon distribution in liquid products was also analyzed (Fig. S3, ESI†). However, when the CNF replaces the AC, although C_{5+} hydrocarbon selectivity increased, the selectivity to by-product CO increased slightly (45.7%). In terms of Fe supported by MPC supports, it exhibits poor selectivity of C_{5+} hydrocarbon and high CO selectivity. In contrast, a Fe-based catalyst supported by the GA can maintain high C_{5+} selectivity. In order to further verify the better performance from the carbonaceous material-supported Fe catalysts, comparison is made with a reference K–Fe/SiO$_2$-C-550 catalyst. In addition to the calcination method, the K–Fe/SiO$_2$ catalyst is also subjected

to a long MH time, and it is found that extending the MH time is also conducive to the formation of higher hydrocarbons (Table S1, ESI†). It suggests that MH is also effective for the metal species carried on the support materials. Notably, Fe supported by carbonaceous materials is more favorable for the efficient conversion of CO_2 to valuable hydrocarbons than inert SiO_2, and the CO_2 hydrogenation performance depends on the types of carbon supports evidently. Besides, in terms of K–Fe/GA-W-10, the effects of the K promoter content on CO_2 were also investigated and compared, as given in Table S2 (ESI†). As shown, with the increase in K promoter content, the selectivity of liquid hydrocarbon is further improved. When the content of K promoter is 7.5%, C_{5+} selectivity is as high as 58.6%. In addition, the superfluous K promoter will further reduce the C_{5+} selectivity. For K promoters, good interfacial contact helps to promote iron active species to catalyze CO_2 to form valuable hydrocarbons. However, excessive K addition will lead to the active sites being covered, leading to poor performance (Table S2, ESI†). The C_{5+} product selectivity is compared with that of typical catalysts reported recently. The corresponding catalysts are simply K promoter–modified Fe catalysts supported by carbon-based materials. Obviously, the designed K–Fe/GA-W-10 catalyst shows a high C_{5+} selectivity compared with traditional catalysts (Table 1).

In general, the obtained catalysts for the reaction need heating pre-treatment, such as calcination, to obtain the desired structure or phase composition. Previous reports have revealed that long-time high-temperature treatment results in several undesired transformations including active-phase sintering and structure failure, which will cause poor catalytic performance, in turn. Previously, it has been reported that the MH method as a facile operation is able to sharply shorten the heating time and promote the dispersion of active species.[34] As a result, the high-temperature pretreatment time for a given catalyst was listed and compared in Table 1. Table 1 only lists the heating processing times above 100 °C. Intuitively, different from the conventional heating procedure, MH treatment can effectively shorten the heating time from several hours to seconds (10 s), which means a shorter preparation cycle and

Table 1 CO_2 conversion and product selectivity from different catalysts

Catalyst	HT[a]	GHSV[b]	H_2/CO_2	P/MPa	T/°C	CO_2 Conv.	CO Sel.	CO-free HCs Sel. (mol%)			Yield (C_{5+})/%
								CH_4	C_2–C_4	C_{5+}	
K–Fe/SiO$_2$-C-550	5 h	4800	2.5	2.0	320	23.1	46.1	14.8	39.6	45.6	5.7
K–Fe/AC-W-10	10 s	4800	2.5	2.0	320	26.3	40.2	16.4	38.9	44.7	7.1
K–Fe/CNF-W-10	10 s	4800	2.5	2.0	320	25.6	45.7	15.2	33.0	51.8	7.2
K–Fe/GA-W-10	10 s	4800	2.5	2.0	320	23.1	42.9	13.7	33.1	53.2	7.0
K–Fe/MPC-W-10	10 s	4800	2.5	2.0	320	24.5	46.2	21.8	37.8	40.4	5.3
K–Fe/SiO$_2$-C-550	>10 h	4800	2.5	2.0	320	18.9	38.7	40.8	31.2	28.0	3.2
FeK/MWNTs[27]	>21 h	9000	3.0	2.0	340	43.6	23.4	27.1	38.5	34.4	11.5
FeK/MPC[30]	>21 h	8000	3.0	2.5	300	37.2	8.4	20.0	36.1	43.9	15.0
KFe/NCNT[31]	>30 h	50 000	3.0	2.5	360	31.8	74.6	76.1	20.1	3.8	0.3
Fe/C-K_2CO_3[40]	>34 h	2400	3.0	2.0	320	37.1	11.5	12.9	41.6	45.5	14.9
FeK/C-1EDA[41]	>24 h	2400	3.0	1.0	300	20.1	31.7	17.2	43.3	39.5	5.4

All the conversion and selectivity data are collected at a stable 6–8 h on stream. [a] Represents the heating time (HT) over 100 °C during catalyst preparation. [b] Unit in mL g_{cat}^{-1} h^{-1}.
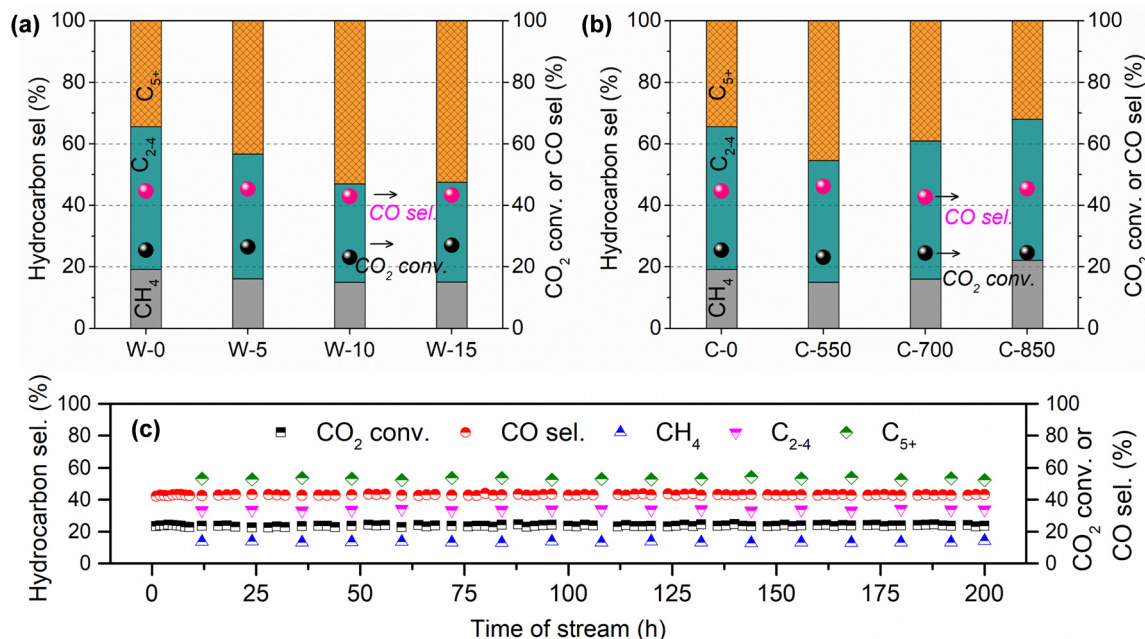
Fig. 1 Effects of microwave time (0–15 s) and calcination temperature (550–850 °C) on CO_2 hydrogenation performance: (a) microwave time, (b) calcination temperature, and (c) catalytic stability. W-0 and C-0 represent the K–Fe/GA sample without any high-temperature treatment, that is, the sample after vacuum drying. Pink and black spheres stand for CO_2 conversion and CO selectivity. Reaction conditions: $H_2/CO_2/Ar = 67.6/27.1/5.3$, $P = 2.0$ MPa, GHSV, 4800 mL g_{cat}^{-1} h^{-1}.

a lower preparation cost. To some extent, the K–Fe/GA-W-10 catalyst obtained by this MH method presents more potential application values.

Meanwhile, the influences of MH time (0–15 s) and calcination temperature (550–850 °C) on CO_2 hydrogenation performance over GA-supported Fe catalysts were also investigated (Fig. 1). As for the K–Fe/GA-W-0 catalyst without any heating treatment, it presents a poor C_{5+} hydrocarbon selectivity. With the prolongation of MH time, the catalytic activity increases slightly while C_{5+} hydrocarbon selectivity increases obviously. When the microwave time reaches 10 seconds, CO_2 hydrogenation shows good performance. On the contrary, calcined catalysts at high temperatures show inferior catalytic hydrogenation performance. Moreover, calcination at high temperatures (850 °C) is not conducive to the formation of C_{5+} hydrocarbon. Catalytic stability is an essential index for the designed catalyst. As depicted in Fig. 1(c), the K–Fe/GA-W-10 catalyst presents benign stability over 200 h on stream. The C_{5+} selectivity stably maintains at 53% throughout the test. These results further indicate that the catalyst prepared by MH has a better application prospect than that of the catalyst prepared by conventional calcination in terms of preparation cost and cycle.

Structural characterization and phase compositions

Fig. S4 and Table S3 (ESI†) depict and summarize the specific surface areas of different Fe-based catalysts based on N_2 physisorption measurement. In Table S3 (ESI†), the specific surface areas for the different Fe-based catalysts follow the sequence of K–Fe/AC (375 m² g⁻¹) > K–Fe/GA-W-10 (91 m² g⁻¹) > K–Fe/MPC-W-10 (69 m² g⁻¹) > K–Fe/SiO₂-C-550

(20 m² g⁻¹) > K–Fe/CNF-W-10 catalyst (19 m² g⁻¹). Fig. S5a (ESI†) shows the *ex situ* XRD patterns of the as-prepared catalysts. For carbon material-supported Fe catalysts, the characteristic diffraction peaks of Fe_3O_4 (JCPDS, 89-0688), an active phase for RWGS reaction, are detected. By contrast, Fe_2O_3 (JCPDS, 89-0598) with a high oxidation state rather than Fe_3O_4 is found in the K–Fe/SiO₂-C-550 catalyst. These results indicate that the carbon-supported Fe catalyst is easier to form active phase by MH treatment. Fig. S5b (ESI†) shows the *ex situ* XRD patterns of the spent catalysts. For K–Fe/SiO₂ catalysts, the main phase after 6 h reaction is metallic Fe (JCPDS, 85-1410). However, the diffraction patterns of Fe_2C (JCPDS, 37-0999) and Fe_5C_2 (JCPDS, 89-2544) are detected in the used K–Fe/AC-W-10 sample. Single Fe_5C_2 (JCPDS, 89-2544) occurs in the K–Fe/CNF-W-10 spent sample. In terms of K–Fe/GA-W-10, the peaks of Fe_2C (JCPDS, 37-0999) and Fe_5C_2 (JCPDS, 89-2544) can be also obviously distinguished. When the support is MPC, the main phase is single Fe_2C (JCPDS, 37-0999). Previously, it has been reported that Fe_2C could be transformed into Fe_5C_2 during the FTS reaction at elevated temperatures.[42] Obviously, the formed carbide phases after reaction depend on the type of support materials and operation conditions. In general, CO_2 hydrogenation forms CO over Fe_3O_4 and then it is catalyzed to heavy hydrocarbons over carbide phases *via* the FTS route.

Fig. 2 and Fig. S6 (ESI†) show the *in situ* XRD patterns of different catalysts under the same operating conditions. For the K–Fe/AC-W-10 catalyst, new iron phases ascribed to FeO (JCPDS, 74-1886) and metallic Fe (JCPDS, 85-1410) appear (Fig. 2(a), 400-0). It provides a direct evidence that Fe_3O_4 was reduced to FeO and then to Fe. As the reduction time expands,
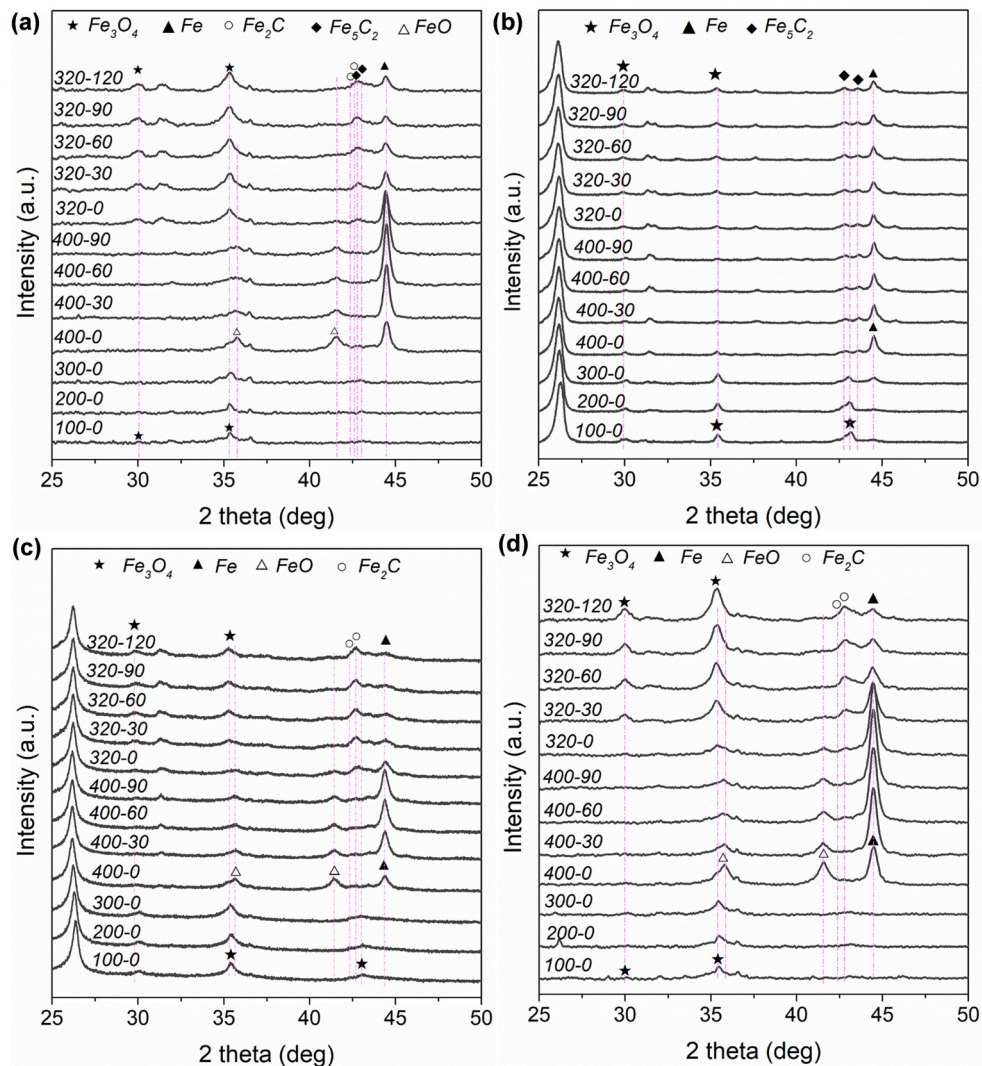
Fig. 2 *In situ* XRD patterns of different catalysts under given conditions: (a) K–Fe/AC-W-10, (b) K–Fe/CNF-W-10, (c) K–Fe/GA-W-10, and (d) K–Fe/MPC-W-10. Notes: the reduction temperature was raised from room temperature to 400 °C and reduced for 90 min in a H_2 atmosphere, then the reaction gas was switched to reaction and phase changes were *in situ* detected. In terms of 320–120, 320 represents 320 °C and 120 stands for 120 min at 320 °C.

the diffraction peak intensity of Fe gradually increases. However, the intensity of metallic Fe decreases when the reactant gas is introduced into the system and a new phase corresponding to Fe_3O_4 appears. Fe_2C and Fe_5C_2 appear with the proceeding of the reaction. Apart from the obvious peaks of Fe_3O_4, the peaks of Fe could be clearly distinguished. For K–Fe/CNF-W-10, the diffraction intensity of Fe changes slightly with the extension of reduction process, and a new carbide (Fe_5C_2) is formed when the reactant gas is introduced. Meanwhile, Fe has the strongest diffraction intensity than that of other phases. It is worth noting that when the reaction proceeds to a certain extent, the change in the diffraction intensity of metallic Fe is almost negligible (Fig. 2(a) and (b)). As far as K–Fe/GA-W-10 is concerned, the content of Fe increases continuously with the proceeding of reduction. However, the diffraction intensity of Fe is sharply decreased after the introduction of reactant gas, and Fe_2C is formed under the atmosphere. This indicates that

carbides are easier to form in this catalyst. With the reaction proceeding, the dominant phases are Fe_3O_4 and Fe_2C, and the diffraction intensity of Fe becomes very low. For K–Fe/MPC-W-10, the diffraction intensity of Fe increases gradually during the reduction process. When the reactant gas is introduced, Fe is oxidized, resulting in the formation of Fe_3O_4, and carbides gradually appear as the reaction proceeds. Different from the above-mentioned catalysts, the diffraction peak of Fe_3O_4 increases gradually with the proceeding of the reaction (Fig. 2(d)). By contrast, the iron species in the K–Fe/SiO$_2$-C-550 catalyst are difficult to be reduced and used for carbonization. The main phases are also Fe_3O_4 and Fe_2O_3 (Fig. S6, ESI†).

Influences of supports and heating treatment operations

The TEM images of the as-prepared catalysts are compared to study the differences in microstructures of active species (Fig. S7, ESI†). Iron species can be uniformly distributed in

the catalyst regardless of the types of Fe-based catalyst supported by carbon materials. Meanwhile, the lattice spacings of 0.253 and 0.296 nm could be attributed to the (311) and (220) planes of Fe_3O_4 (Fig. S7, ESI†). However, for K–Fe/CNF-W-10 and K–Fe/GA-W-10 samples, iron species are obviously covered by a graphitic carbon layer (Fig. S7b and c, ESI†). In particular, K–Fe/GA-W-10 presents a small-size distribution with *ca.* 5 nm. The HAADF-TEM images and the corresponding elemental mapping images indicate that the elements are evenly distributed without any high-temperature treatment (K–Fe/GA-W-0, Fig. 3(a)). In contrast, the element distributions in the K–Fe/GA-W-10 sample after MH treatment are more uniform (K–Fe/GA-W-10, Fig. 3(b), and Fig. S8, ESI†).

Fig. 3(c)–(f) and Fig. S9, S10 (ESI†) show the TEM images and the corresponding crystallite sizes of the used samples. After the reaction, K–Fe/AC-W-10 exhibits a core–shell structure, in which the shell is a carbon layer and the core is carbides. The lattice planes of Fe_2C (−311) are detected as the main active phases. The particle size of iron species is about 20 nm (Fig. 3(a) and Fig. S10a, ESI†). A similar structure also appears in the K–Fe/CNF-W-10 sample with a larger size (50 nm), and the main phase is Fe_5C_2 (510). However, for the used

K–Fe/GA-W-10 sample, there is no core–shell structure. Notably, iron species present small particle sizes, usually less than 5 nm, which is different from that of other catalysts. For the remaining catalysts, the particle sizes of iron active species increase significantly after the reaction (Fig. S7 and S10, ESI†). In addition, the main phase is Fe_2C (121) for K–Fe/GA-W-10. For the K–Fe/MPC-W-10 catalyst, the core–shell structure also appears after the reaction, and the particle sizes change from 40 to 100 nm (Fig. 3(d)). Similar to the K–Fe/GA-W-10 sample, Fe_2C (121) remains the dominant phase, which is well consistent with the XRD analysis (Fig. S5, ESI† and Fig. 3(d)). Besides, based on the XRD data shown in Fig. 2, the particle sizes of different catalysts in various time periods are compared and listed in Table S4 (ESI†). Obviously, with the process of reduction, the particle size of iron species increased gradually, and then the catalytic particle meditation decreased when switching to reaction gas. With the extension of the reaction time, the active phase particles gradually increased and stabilized. Similar to the TEM results, the GA-supported catalyst had the smallest particle size of iron species. These findings indicate that the utilization of GA support is conducive to the carburization of Fe_3O_4, producing small particles of active
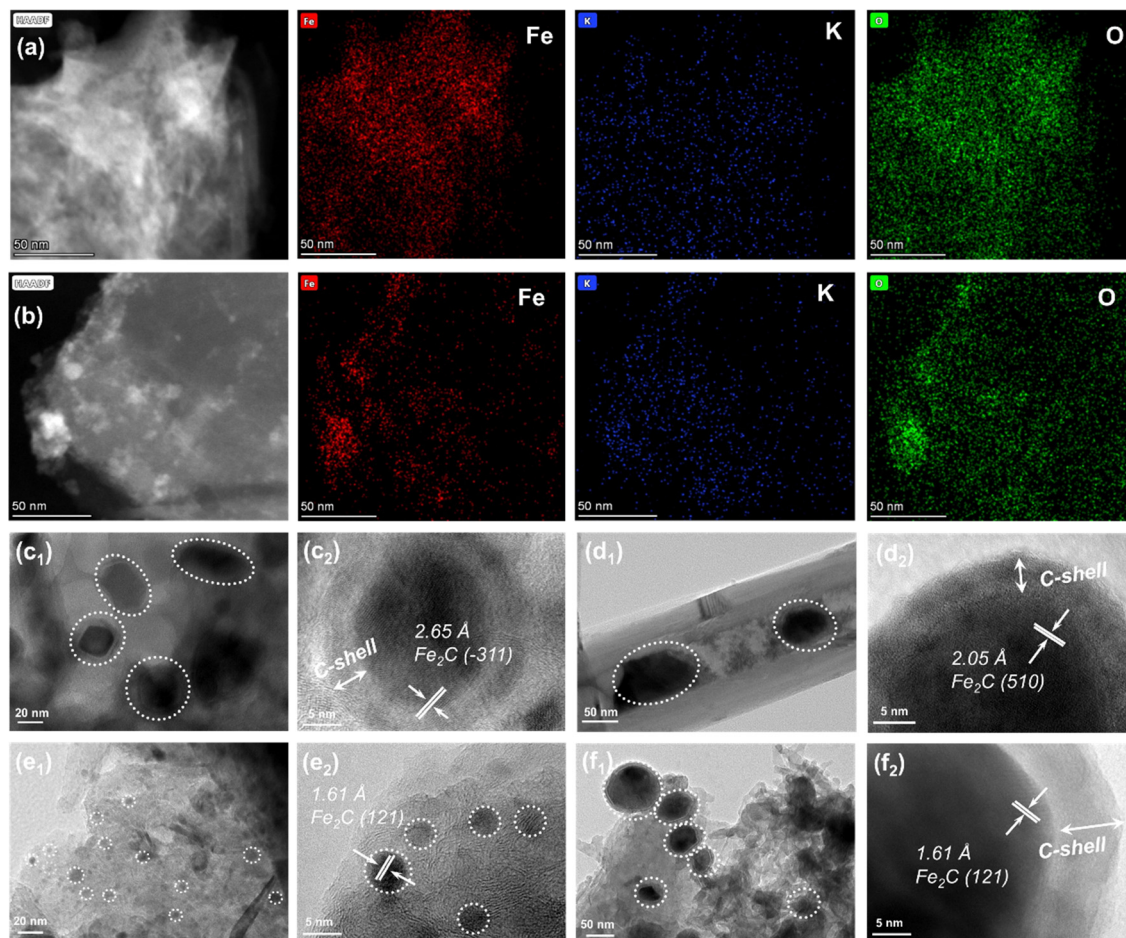

Fig. 3   HAADF-TEM images and the corresponding elemental mapping images of (a) K–Fe/GA-W-0 and (b) K–Fe/GA-W-10 catalysts. TEM and HR-TEM images of spent catalysts: (c) K–Fe/AC-W-10, (d) K–Fe/CNF-W-10, (e) K–Fe/GA-W-10, and (f) K–Fe/MPC-W-10 catalysts.

phases and providing more contact interfaces between active sites and feed gases. Moreover, GA-supported Fe nanoparticles are more conducive to maintaining the small particle size. By contrast, for the used K–Fe/SiO$_2$-C-550, Fe$_3$O$_4$ (220) rather than carbides as the active phase is detected and the sizes counter at 100 nm, which is also confirmed by XRD results (Fig. S6 and S9, ESI†).

The reduction and CO$_2$ adsorption properties were investigated by H$_2$-TPR and CO$_2$-TPD experiments, respectively (Fig. S11 and S12, ESI†). Different from the inert SiO$_2$ support, carbon material-supported Fe nanoparticles are easier to be reduced. Thereinto, the iron species in the K–Fe/AC-W-10 catalyst are more easily reduced, followed by K–Fe/GA-W-10 and K–Fe/MPC-W-10, and finally the K–Fe/CNF-W-10 sample (Fig. S11, ESI†), which is consistent with the results from *in situ* XRD patterns (Fig. 2). As from H$_2$-TPR, improved reduction behavior can promote the formation of Fe phase and facilitate the *in situ* formation of active phase. In general, from CO$_2$-TPD, the desorption temperature below 650 °C could be assigned to CO$_2$ chemisorbed peaks and physical adsorption peaks, while the peaks above 650 °C are due to the degradation of carbonaceous materials. Correspondingly, according to the results of CO$_2$-TPD, CO$_2$ raw molecules could interact well with iron species over K–Fe/GA-W-10 and K–Fe/MPC-W-10 catalysts compared to the remaining samples (Fig. S12, ESI†).

The effects of MH time (0–15 s) on the catalyst structures were investigated (Fig. S13, ESI†). For the sample after vacuum drying without any MH treatment, it shows large bulk irregular size structures. With the extension of MH time, bulk structures become small-sized particles, given that the microwave heating action is strengthened. When the microwave time exceeds 10 s, the catalyst particles are obviously reduced and further change is not obvious (*ca.* 5 nm), and more graphitic carbon layers appear around the metal species. This indicates that the suitable MH time is beneficial for the formation of small-sized iron species. In addition, TEM was performed on the

used catalysts treated with different microwave durations (Fig. S14, ESI†). It can be found that a suitable microwave heat treatment duration (10 s) can effectively tune the particle size of active species. The chain growth reaction is a structurally sensitive reaction, and the smaller particle size is helpful to improve the catalytic performance. Meanwhile, in order to further compare the difference between MH and traditional heating methods such as calcination, the microwave and calcined samples were compared (Fig. S15, ESI†). Apparently, high calcination temperatures (700 and 850 °C) render the formation of large particles (Fig. S15b and c, ESI†). Although an appropriate low calcination temperature (550 °C) brings uniform particles, MH treatment is more conducive to the formation of small-sized iron species with high exposed active surface. In addition, the samples with various MH time periods present similar XRD patterns, indicating that MH can effectively promote the uniform dispersion of metal particles (Fig. S16, ESI†). By contrary, the corresponding precursor samples (K–Fe/GA-W-0 or K–Fe/GA-C-0) show obvious differences after the utilization of high-temperature calcination (Fig. S17, ESI†). With the increase in calcination temperature, metallic Fe species appear rather than Fe$_3$O$_4$ in an inert N$_2$ atmosphere. Previously, similar findings were reported for NiO supported on graphene, and this phenomenon may be ascribed to the action of graphitic carbons and hydroxyl groups.[43,44] Clearly, rapid heating and slow high calcination can induce different process changes in the catalyst precursor period. It shows that the MH method is not only fast and efficient, but also more beneficial to the preparation and synthesis of specific catalysts.

The phase composition and content of surface species were also investigated by XPS (Fig. 4, Fig. S18–S20, and Tables S5–S7, ESI†). As shown in Fig. S18, the XPS spectrum of the Fe 2p region of all samples can be fitted with two spin–orbit doublets corresponding to the Fe 2p$_{1/2}$ and Fe 2p$_{3/2}$ peaks and the corresponding satellite peaks of Fe^{2+} and Fe^{3+}, which are typical characteristic peaks of Fe$_3$O$_4$.[45] The iron nanoparticles
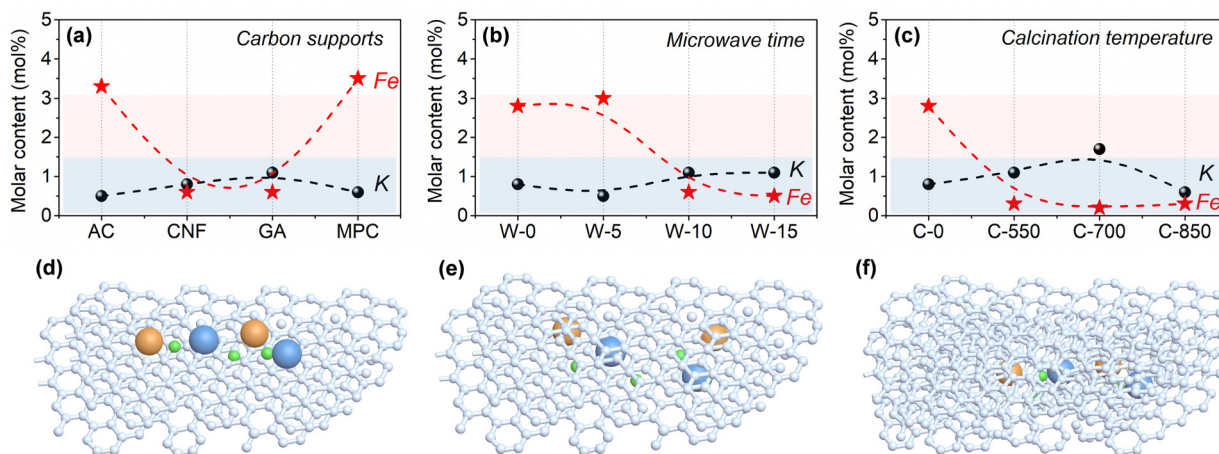

Fig. 4 Surface element compositions of the as-prepared catalysts: (a) iron catalysts supported by various carbon materials; (b) K–Fe/GA catalysts treated by different MH times; (c) K–Fe/GA catalysts treated by different calcination temperatures using a tube furnace; (d) active metal species supported on the surface of support, *e.g.* AC and MPC; (e) the active metal encapsulated with appropriate graphitic carbon layers, *e.g.* W-10 and W-15; and (f) active metal species encapsulated with more graphitic carbon layers, *e.g.* C-550, C-700 and C-850.

supported by GA and CNF have a higher surface Fe(II) content (Fig. S18, ESI†). As mentioned above, the K promoter promotes the formation of heavy hydrocarbons.

Encapsulation structure of iron nanoparticles with a carbon shell or layers

According to Fig. 4 and Table S5 (ESI†), the surface contents of iron species in K–Fe/GA-W-10 and K–Fe/CNF-W-10 samples are lower than those of K–Fe/AC-W-10 and K–Fe/MPC-W-10. In fact, the actual surface contents are much lower than the theoretical level, indicating that large amounts of iron species are encapsulated by carbon supports. In addition, with the extension of MH time, the surface content of iron species on the surface first decreases and then becomes constant, while the contents of C show an opposite trend (Table S6, ESI†). Unlike the convenient MH treatment, the surface content of iron species after calcination treatment is obviously lower than that of MH (Table S7, ESI†). Although low calcination temperatures are also conducive to the formation of uniform iron species, the inferior CO absorption and slightly large size to active Fe phase (Fig. S14 and S21; ESI† data from the difference of encapsulation structures) are unfavorable to improve the catalytic performance. These findings clearly reveal that carbon support types and heating methods can affect the surface contents of active iron species. Combined with the above-mentioned results, it can be considered that the metal iron species are encapsulated in the GA support structures or graphitic carbon layers. Similarly, You *et al.* reported that the hexagonal phase of Pd nanomaterials can be well encapsulated by graphite in terms of graphite templating effects and size effects.[46]

Different from the K–Fe/SiO₂-C-550 reference catalyst, the content of Fe(II) is higher for carbon-supported Fe catalysts (Fig. S19, ESI†), an active phase for catalyzing CO_2 molecule hydrogenation. According to the C 1s and O 1s spectra, there are more C–C species and low content of C–O/C═O species, indicating that more adsorption species are converted into hydrocarbon products over K–Fe/GA-W-10 (Fig. S20, ESI†). Notably, the low intensity of Fe species especially for K–Fe/GA-W-10 indicates that iron species are encapsulated into the support or carbon shells (Fig. 3 and Fig. S7, S10, ESI†). This phenomenon could also be confirmed based on the surface content analysis of iron species (Table S8, ESI†). As for the K–Fe/GA-W-10 catalyst, there is no metal species coated by a carbon shell, thus Fe nanoparticles are more likely to be encapsulated in the graphene support or graphitic carbon layers. Based on this discussion, the schematic diagram of the active iron species in/on the support materials is depicted (Fig. 4(d)–(f)). For the used samples, the data of K and Fe surface content were also compared, as shown in Fig. S21 (ESI†). Similar to the samples before the reaction, the samples after reaction showed the same trend, indicating that the packaging structure was still obvious in the reaction process, and gradually appeared for AC- and MPC-supported iron catalysts. As shown in Fig. S22 (ESI†), CO-TPD experiments were further conducted to investigate the Fe accessibility. Compared with K–Fe/GA-W-0, the CO adsorption intensity decreases with

the assistance of microwave heating. By contrast, the catalyst with calcination treatment presents inferior CO adsorption at low temperatures. Moreover, the desorption temperature of CO in the high-temperature region increases further. These results further support these findings to some extent (Fig. 4). In addition, the K 2p XPS spectra of used samples were compared, as shown in Fig. S23 (ESI†). As indicated, with the increase in K content, the binding energy shifts to a high binding energy location, indicating that K donates electrons to iron species. Generally, the change in electronic density enhances the strength of the Fe–C bond. In addition, the K promoter can suppress olefin secondary hydrogenation and then promote the formation of heavy olefin-rich hydrocarbons. Meanwhile, it is reported that the contact angle of H_2O on graphenes is significantly higher than that on graphite, which indicates that graphenes have the most hydrophobic surfaces with very weak interactions with the H_2O molecules.[47] Xu *et al.* also reported that nanoscale zero-valent iron prepared by a carbothermal reduction method catalyzed the amorphous carbon to form hydrophobic graphitic layers.[48] Generally, the presence of H_2O molecules can oxidize the active phase and thus reduce the CO_2 hydrogenation performance. Quick water removal from hydrogenation processes plays a crucial role for promoting CO_x hydrogenation.[25,49] The water contact angle test shows that the graphene-supported catalyst has benign hydrophobicity, and the hydrophobicity of K–Fe/GA after MH treatment is enhanced (Fig. S24, ESI†). However, after the reaction, the hydrophilic and hydrophobic properties will change with the occurrence of the reaction. Thus, Fe nanoparticles encapsulated in the hydrophobic graphene support or graphitic carbon layers could be an ideal sample for catalyzing CO_2 hydrogenation.

The differences in the structure of the as-prepared catalysts with different heating manners were further assessed by Raman spectroscopy. In terms of the Raman spectra of three catalysts, two peaks can be clearly seen at around 1580 and 1350 cm⁻¹, which can be attributed to the G band and the D band, respectively (Fig. S25, ESI†).[22,50] Thereinto, the intensity of the G band is relative to the growth of graphitic carbons, while the intensity of the D band is a feature for disordered graphite including defects and sp³-hybridized carbons; then, the relative intensity (I_D/I_G) of the D band and G band can reflect the defect sites or graphitization degree. Obviously, the utilization of different heating methods shows slight influence on the defect structures of supports (Table S9, ESI†), which also means that the GA-loaded iron nanoparticles have benign thermal stability during preparation steps. This finding shows that the GA-supported iron catalyst has good stability, and the difference in catalytic performance is mainly due to the formation of the package structure. In addition, the spent K–Fe/GA-W-10 catalyst obtained after 200 h of reaction was further characterized by TEM. With the prolongation of reaction time, the particle size of the catalyst increases obviously (Fig. 2 and Fig. S26, ESI†). Moreover, the crystalline Fe_5C_2 core is covered with an amorphous shell, which is distinctly different from the previous catalyst obtained after 6 h of reaction (Fig. S26, ESI†). The core (iron species)–shell (carbon) configuration is a typical
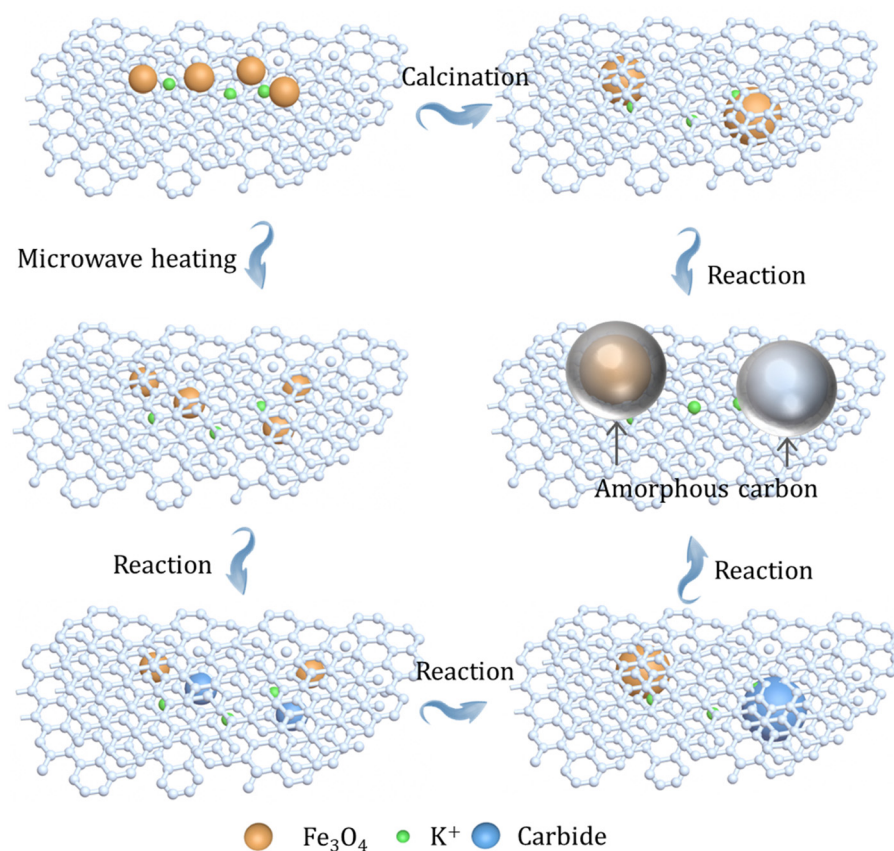
Fig. 5 Schematic diagram of the changes in active iron species microenvironment on different catalysts after high-temperature heating treatment and reaction.

structure for FTS Fe-based catalysts.[40,51–53] Similarly, Kim et al. also reported this phenomenon for the Na–Fe$_3$O$_4$/CNT after 24 h of reaction.[54] Chernyak et al. reported the formation of a carbide core–amorphous carbon–graphitic carbon structure.[55] Zhang et al. reported that the presence of a graphene shell could inhibit the sintering and agglomeration of active phases, and reduce the negative effects of water by blocking the contact between H$_2$O and active phases.[56] It can be inferred that when the catalyst particle size is small and coated by graphitic carbon layers, the amorphous carbon is not easily formed on the surface of active phases (Fig. 2 and Fig. S10, ESI†). However, when the particle size increases significantly, the catalyst particles show a tendency to form the amorphous carbon (Fig. S26, ESI†). The presence of the graphitic carbon or amorphous carbon can provide a good stable carbon environment for active carbides, making the catalyst exhibit good catalytic performance (Fig. 5). Previously, Gupta et al. reported a carbon-coated core–shell iron nanocatalyst for efficient CO$_2$ hydrogenation, and found that the presence of a carbon shell could prevent rapid deactivation via hindering the aggregation of particles and enhance C$_{2+}$ olefin selectivity.[57] Besides, porous graphene-confined Fe catalysts also presented benign activity and excellent stability for CO2 hydrogenation to C$_{2+}$ olefins, which is ascribed to the confinement effect.[58]

Conclusions

Compared with AC-, MPC-, and CNF-supported iron catalysts, the GA-supported catalyst treated by simple MH presents a relatively small size with high exposed surface of active species and uniform dispersion. In addition, GA-supported iron also presents a benign carburization behavior. In terms of GA support, small-size active precursors are coated by graphitic carbon layers. With the introduction of reaction gases, an amorphous carbon shell is formed on the surface of active carbides for AC-, MPC-, and CNF-supported catalysts. For GA-supported iron catalysts, the presence of graphitic carbon layers can slow down the particle sintering during CO$_2$ hydrogenation. By contrast, classic high calcination temperatures will form large particles of active precursors, which is not conducive to promote CO$_2$ hydrogenation. With the increase in particle size, these active carbides are coated with the amorphous carbon (K–Fe/AC-W-10). In this process, the formed H$_2$O can keep a distance with the active carbide or is quickly removed owing to the constant presence of hydrophobic carbon shells (graphenes, graphitic carbons, and amorphous carbons), which are helpful to improve the catalytic performance.

Under such a space-confined carbon environment, the active iron sites are probable to express unique catalytic performance, which finally results in a favorable performance as we observed.

When the MH time is 10 s, the K–Fe/GA-W-10 catalyst shows 53.2% C_{5+} selectivity at a CO_2 conversion of 23.1%, and the test of 200 h reaction indicates good stability for CO_2 hydrogenation. Carbon material-supported iron nanoparticles with the utilization of rapid MH provide a new and facile strategy for CO_2 hydrogenation to produce high value-added products such as heavy hydrocarbons. Excellent absorbents of microwaves such as GA act as benign supports for catalyzing CO_2 hydrogenation, and MH distinctly shortens the manufacturing cycle and production cost, which is an important factor in industrial production.

Conflicts of interest

The authors declare that they have no known competing financial interests or personal relationships that could have appeared to influence the work reported in this paper.

Acknowledgements

References

1 R.-P. Ye, J. Ding, W. Gong, M. D. Argyle, Q. Zhong, Y. Wang, C. K. Russell, Z. Xu, A. G. Russell, Q. Li, M. Fan and Y.-G. Yao, CO_2 hydrogenation to high-value products *via* heterogeneous catalysis, *Nat. Commun.*, 2019, **10**, 5698.

2 W. Wang, S. Wang, X. Ma and J. Gong, Recent advances in catalytic hydrogenation of carbon dioxide, *Chem. Soc. Rev.*, 2011, **40**(7), 3703–3727.

3 E. V. Kondratenko, G. Mul, J. Baltrusaitis, G. O. Larrazábalc and J. Pérez-Ramírez, Status and perspectives of CO_2 conversion into fuels and chemicals by catalytic, photocatalytic and electrocatalytic processes, *Energy Environ. Sci.*, 2013, **6**, 3112–3135.

4 W. Zhou, K. Cheng, J. Kang, C. Zhou, V. Subramanian, Q. Zhang and Y. Wang, New horizon in C1 chemistry: breaking the selectivity limitation in transformation of syngas and hydrogenation of CO_2 into hydrocarbon chemicals and fuels, *Chem. Soc. Rev.*, 2019, **48**, 3193–3228.

5 J. Zhu, G. Zhang, W. Li, X. Zhang, F. Ding, C. Song and X. Guo, Deconvolution of the Particle Size Effect on CO_2 Hydrogenation over Iron-Based Catalysts, *ACS Catal.*, 2020, **10**(13), 7424–7433.

6 L. Guo, J. Sun, Q. Ge and N. Tsubaki, Recent Advances in Direct Catalytic Hydrogenation of Carbon Dioxide to Valuable C2+ Hydrocarbons, *J. Mater. Chem. A*, 2018, **6**, 23244–23262.

7 Y. Ni, Z. Chen, Y. Fu, Y. Liu, W. Zhu and Z. Liu, Selective Conversion of CO_2 and H_2 into Aromatics, *Nat. Commun.*, 2018, **9**, 3457.

8 H. Li, C. Qiu, S. Ren, Q. Dong, S. Zhang, F. Zhou, X. Liang, J. Wang, S. Li and M. Yu, Na^+-gated water-conducting nanochannels for boosting CO_2 conversion to liquid fuels, *Science*, 2020, **367**, 667–671.

9 J. Graciani, K. Mudiyanselage, F. Xu, A. E. Baber, J. Evans, S. D. Senanayake, D. J. Stacchiola, P. Liu, J. Hrbek, J. F. Sanz and J. A. Rodriguez, Highly active copper-ceria and copper-ceria-titania catalysts for methanol synthesis from CO_2, *Nature*, 2014, **345**, 6196.

10 J. Wei, Q. Ge, R. Yao, Z. Wen, C. Fang, L. Guo, H. Xu and J. Sun, Directly converting CO_2 into a gasoline fuel, *Nat. Commun.*, 2017, **8**, 15174–15181.

11 C. Zhou, J. Shi, W. Zhou, K. Cheng, Q. Zhang, J. Kang and Y. Wang, Highly Active ZnO–ZrO$_2$ Aerogels Integrated with H-ZSM-5 for Aromatics Synthesis from Carbon Dioxide, *ACS Catal.*, 2020, **10**, 302–310.

12 P. Gao, S. Li, X. Bu, S. Dang, Z. Liu, H. Wang, L. Zhong, M. Qiu, C. Yang, J. Cai, W. Wei and Y. Sun, Direct conversion of CO_2 into liquid fuels with high selectivity over a bifunctional catalyst, *Nat. Chem.*, 2017, **9**, 1019–1024.

13 Z. He, M. Cui, Q. Qian, J. Zhang, H. Liu and B. Han, Synthesis of liquid fuel *via* direct hydrogenation of CO_2, *Proc. Natl. Acad. Sci. U. S. A.*, 2019, **116**, 12654–12659.

14 R. McGinnis, CO_2-to-Fuels Renewable Gasoline and Jet Fuel Can Soon Be Price Competitive with Fossil Fuels, *Joule*, 2020, **4**, 1–3.

15 L. Zhang, Y. Dang, X. Zhou, P. Gao, A. Petrus van Bavel, H. Wang, S. Li, L. Shi, Y. Yang, E. I. Vovk, Y. Gao and Y. Sun, Direct conversion of CO2 to a jet fuel over CoFe alloy catalysts, *Innovation*, 2021, **2**(4), 100170.

16 G. Song, M. Li, P. Yan, M. A. Nawaz and D. Liu, High Conversion to Aromatics *via* CO_2-FT over a CO-Reduced Cu–Fe$_2$O$_3$ Catalyst Integrated with HZSM-5, *ACS Catal.*, 2020, **10**(19), 11268–11279.

17 X. Dong, F. Li, N. Zhao, F. Xiao, J. Wang and Y. Tan, CO_2 hydrogenation to methanol over Cu/ZnO/ZrO$_2$ catalysts prepared by precipitation-reduction method, *Appl. Catal., B*, 2016, **191**, 8–17.

18 L. Tan, P. Zhang, Y. Cui, Y. Suzuki, H. Li, L. Guo, G. Yang and N. Tsubaki, Direct CO_2 hydrogenation to light olefins by suppressing CO by-product formation, *Fuel Process. Technol.*, 2019, **196**, 106174.

19 M. Amoyal, R. Vidruk-Nehemya, M. V. Landau and M. Herskowit, Effect of potassium on the active phases of Fe catalysts for carbon dioxide conversion to liquid fuels through hydrogenation, *J. Catal.*, 2017, **348**, 29–39.

20 P. Zhai, C. Xu, R. Gao, X. Liu, M. Li, W. Li, X. Fu, C. Jia, J. Xie, M. Zhao, X. Wang, Y.-W. Li, Q. Zhang, X.-D. Wen and D. Ma, Highly tunable selectivity for syngas-derived alkenes over Zinc and Sodium-modulated Fe$_5$C$_2$ catalyst, *Angew. Chem., Int. Ed.*, 2016, **55**, 9902.

21 R. Yao, J. Wei, Q. Ge, J. Xu, Y. Han, Q. Ma, H. Xu and J. Sun, Monometallic iron catalysts with synergistic Na and S for

higher alcohols synthesis *via* CO_2 hydrogenation, *Appl. Catal., B*, 2021, **298**, 120556.

22 L. Guo, P. Zhang, Y. Cui, G. Liu, J. Wu, G. Yang, Y. Yoneyama and N. Tsubaki, One-Pot Hydrothermal Synthesis of Nitrogen Functionalized Carbonaceous Material Catalysts with Embedded Iron Nanoparticles for CO_2 Hydrogenation, *ACS Sustainable Chem. Eng.*, 2019, **7**, 8331–8339.

23 Y. H. Choi, E. C. Ra, E. H. Kim, K. Y. Kim, Y. J. Jang, K.-N. Kang, S. H. Choi, J.-H. Jang and J. S. Lee, Sodium-Containing Spinel Zinc Ferrite as a Catalyst Precursor for the Selective Synthesis of Liquid Hydrocarbon Fuels, *ChemSusChem*, 2017, **10**, 4764–4770.

24 L. Guo, J. Sun, X. Ji, J. Wei, Z. Wen, R. Yao, H. Xu and Q. Ge, Directly converting carbon dioxide to linear α-olefins on bio-promoted catalysts, *Commun. Chem.*, 2018, **1**, 11.

25 L. Guo, J. Li, Y. Cui, R. Kosol, Y. Zeng, G. Liu, J. Wu, T. Zhao, G. Yang, L. Shao, P. Zhan, J. Chen and N. Tsubaki, Spinel-structure catalyst catalyzing CO_2 hydrogenation to full spectrum alkenes with an ultra-high yield, *Chem. Commun.*, 2020, **56**, 9372–9375.

26 J. Wei, J. Sun, Z. Wen, C. Fang, Q. Ge and H. Xu, New insights into the effect of sodium on Fe_3O_4-based nanocatalysts for CO_2 hydrogenation to light olefins, *Catal. Sci. Technol.*, 2016, **6**(13), 4786–4793.

27 S. Wang, T. Wu, J. Lin, Y. Ji, S. Yan, Y. Pei, S. Xie, B. Zong and M. Qiao, Iron–Potassium on Single-Walled Carbon Nanotubes as Efficient Catalyst for CO_2 Hydrogenation to Heavy Olefins, *ACS Catal.*, 2020, **10**(11), 6389–6401.

28 M. Zhu, P. Tian, R. Kurtz, T. Lunkenbein, J. Xu, R. Schlögl, I. E. Wachs and Y.-F. Han, Strong Metal–Support Interactions between Copper and Iron Oxide during the High-Temperature Water-Gas Shift Reaction, *Angew. Chem., Int. Ed.*, 2019, **58**(27), 9083–9087.

29 S. Li, Y. Xu, Y. Chen, W. Li, L. Lin, M. Li, Y. Deng, X. Wang, B. Ge, Y. Ce, S. Yao, J. Xie, Y. Li, X. Liu and D. Ma, Tuning the Selectivity of Catalytic Carbon Dioxide Hydrogenation over Iridium/Cerium Oxide Catalysts with a Strong Metal–Support Interaction, *Angew. Chem., Int. Ed.*, 2017, **56**(36), 10761–10765.

30 S.-M. Hwang, C. Zhang, S. J. Han, H.-G. Park, Y. T. Kim, S. Yang, K.-W. Jun and S. K. Kim, Mesoporous carbon as an effective support for Fe catalyst for CO_2 hydrogenation to liquid hydrocarbons, *J. CO2 Util.*, 2020, **37**, 65–73.

31 P. Kangvansura, L. M. Chew, C. Kongmark, P. Santawaja, H. Ruland, W. Xia, H. Schulz, A. Worayingyong and M. Muhler, Effects of Potassium and Manganese Promoters on Nitrogen-Doped Carbon Nanotube-Supported Iron Catalysts for CO_2 Hydrogenation, *Engineering*, 2017, **3**(3), 385–392.

32 Y. Cheng, J. Lin, K. Xu, H. Wang, X. Yao, Y. Pei, S. Yan, M. Qiao and B. Zong, Fischer-Tropsch Synthesis to Lower Olefins over Potassium-Promoted Reduced Graphene Oxide Supported Iron Catalysts, *ACS Catal.*, 2016, **6**(1), 389–399.

33 H. Xiong, L. L. Jewell and N. J. Coville, Shaped Carbons As Supports for the Catalytic Conversion of Syngas to Clean Fuels, *ACS Catal.*, 2015, **5**(4), 2640–2658.

34 L. Guo, Z. Guo, J. Liang, X. Yong, S. Sun, W. Zhang, J. Sun, T. Zhao, J. Li, Y. Cui, B. Zhang, G. Yang and N. Tsubaki, Quick Microwave Assembling Nitrogen-Regulated Graphene Supported Iron Nanoparticles for Fischer-Tropsch Synthesis, *Chem. Eng. J.*, 2022, **429**, 132063.

35 F. Qin and C. Brosseau, A review and analysis of microwave absorption in polymer composites filled with carbonaceous particles, *J. Appl. Phys.*, 2012, **111**(6), 061301.

36 R. Kumar, S. Sahoo, E. Joanni and R. K. Singh, A review on the current research on microwave processing techniques applied to graphene-based supercapacitor electrodes: An emerging approach beyond conventional heating, *J. Energy Chem.*, 2022, **74**, 252–282.

37 R. Jakhar, J. E. Yap and R. Joshi, Microwave reduction of graphene oxide, *Carbon*, 2020, **170**, 277–293.

38 J. A. Menéndez, A. Arenillas, B. Fidalgo, Y. Fernández, L. Zubizarreta, E. G. Calvo and J. M. Bermúdez, Microwave heating processes involving carbon materials, *Fuel Process. Technol.*, 2010, **91**(1), 1–8.

39 L. Guo, X. Gao, W. Gao, H. Wu, X. Wang, S. Sun, Y. Wei, Y. Kugue, X. Guo, J. Sun and N. Tsubaki, High-yield production of liquid fuels in CO_2 hydrogenation on a zeolite-free Fe-based catalyst, *Chem. Sci.*, 2023, **14**(1), 171–178.

40 Y. Han, C. Fang, X. Ji, J. Wei, Q. Ge and J. Sun, Interfacing with Carbonaceous Potassium Promoters Boosts Catalytic CO_2 Hydrogenation of Iron, *ACS Catal.*, 2020, **10**(20), 12098–12108.

41 R. Kosol, L. Guo, N. Kodama, P. Zhang, P. Reubroycharoen, T. Vitidsant, A. Taguchi, T. Abe, J. Cheng, G. Yang, Y. Yoneyama and N. Tsubaki, Iron Catalysts Supported on Nitrogen Functionalized Carbon for Improved CO_2 Hydrogenation Performance, *Catal. Commun.*, 2021, **149**, 106216.

42 X.-P. Fu, W.-Z. Yu, C. Ma, J. Lin, S.-Q. Sun, S.-Q. Li, P.-N. Ren, F.-Y. Jia, M.-Y. Li, W.-W. Wang, X. Wang, C.-J. Jia, K. Wu, R. Si and C.-H. Yan, Supported Fe_2C catalysts originated from Fe_2N phase and active for Fischer-Tropsch synthesis, *Appl. Catal., B*, 2021, **284**, 119702.

43 Y. J. Mai, J. P. Tu, C. D. Gu and X. L. Wang, Graphene anchored with nickel nanoparticles as a high-performance anode material for lithium ion batteries, *J. Power Sources*, 2012, **209**, 1–6.

44 L. Wang, Y. Jiao, S. Yao, P. Li, R. Wang and G. Chen, MOF-derived NiO/Ni architecture encapsulated into N-doped carbon nanotubes for advanced asymmetric supercapacitors, *Inorg. Chem. Front.*, 2019, **6**(6), 1553–1560.

45 Y. Chen, L. Ma, R. Zhang, R. Ye, W. Liu, J. Wei, V. V. Ordomsky and J. Liu, Carbon-supported Fe catalysts with well-defined active sites for highly selective alcohol production from Fischer-Tropsch synthesis, *Appl. Catal., B*, 2022, **312**, 121393.

46 R. You, Z. Wu, J. Yu, F. Wang, S. Chen, Z.-K. Han, W. Yuan, H. Yang and Y. Wang, Revealing Surface Restraint-Induced Hexagonal Pd Nanocrystals *via* In Situ Transmission Electron Microscopy, *Nano Lett.*, 2022, **22**(11), 4333–4339.

47 S. O. Moussa, L. S. Panchakarla, M. Q. Ho and M. S. El-Shall, Graphene-Supported, Iron-Based Nanoparticles

for Catalytic Production of Liquid Hydrocarbons from Synthesis Gas: The Role of the Graphene Support in Comparison with Carbon Nanotubes, *ACS Catal.*, 2014, **4**, 535–545.

48 Q. Xu, X. Liu, D. Lai, Z. Xing, P. Ndagijimana, Z. Li and Y. Wang, One-step synthesis of nanoscale zero-valent iron modified hydrophobic mesoporous activated carbon for efficient removal of bulky organic pollutants, *J. Cleaner Prod.*, 2022, **356**, 131854.

49 W. Fang, C. Wang, Z. Liu, L. Wang, L. Liu, H. Li, S. Xu, A. Zheng, X. Qin, L. Liu and F.-S. Xiao, Physical mixing of a catalyst and a hydrophobic polymer promotes CO hydrogenation through dehydration, *Science*, 2022, **377**, 406–410.

50 H. Xiong, M. Moyo, M. A. Motchelaho, Z. N. Tetana, S. M. A. Dube, L. L. Jewell and N. J. Coville, Fischer-Tropsch synthesis: Iron catalysts supported on N-doped carbon spheres prepared by chemical vapor deposition and hydrothermal approaches, *J. Catal.*, 2014, **311**, 80–87.

51 C. Ma, W. Zhang, Q. Chang, X. Wang, H. Wang, H. Chen, Y. Wei, C. Zhang, H. Xiang, Y. Yang and Y. Li, θ-Fe$_3$C dominated Fe@C core–shell catalysts for Fischer-Tropsch synthesis: Roles of θ-Fe$_3$C and carbon shell, *J. Catal.*, 2021, **393**, 238–246.

52 C. Wei, W. Tu, L. Jia, Y. Liu, H. Lian, P. Wang and Z. Zhang, The evolutions of carbon and iron species modified by Na and their tuning effect on the hydrogenation of CO$_2$ to olefins, *Appl. Surf. Sci.*, 2020, **525**, 146622.

53 S. Lyu, C. Liu, G. Wang, Y. Zhang, J. Li and L. Wang, Structural evolution of carbon in an Fe@C catalyst during the Fischer–Tropsch synthesis reaction, *Catal. Sci. Technol.*, 2019, **9**(4), 1013–1020.

54 K. Y. Kim, H. Lee, W. Y. Noh, J. Shin, S. J. Han, S. K. Kim, K. An and J. S. Lee, Cobalt Ferrite Nanoparticles to Form a Catalytic Co–Fe Alloy Carbide Phase for Selective CO$_2$ Hydrogenation to Light Olefins, *ACS Catal.*, 2020, **10**(15), 8660–8671.

55 S. A. Chernyak, A. S. Ivanov, S. V. Maksimov, K. I. Maslakov, O. Y. Isaikina, P. A. Chernavskii, R. V. Kazantsev, O. L. Eliseev and S. S. Savilov, Fischer-Tropsch synthesis over carbon-encapsulated cobalt and iron nanoparticles embedded in 3D-framework of carbon nanotubes, *J. Catal.*, 2020, **389**, 270–284.

56 P. Zhang, F. Han, J. Yan, X. Qiao, Q. Guan and W. Li, N-doped ordered mesoporous carbon (N-OMC) confined Fe$_3$O$_4$–FeC$_x$ heterojunction for efficient conversion of CO$_2$ to light olefins, *Appl. Catal., B*, 2021, **299**, 120639.

57 S. Gupta, V. K. Jain and D. Jagadeesan, Fine Tuning the Composition and Nanostructure of Fe-Based Core–Shell Nanocatalyst for Efficient CO$_2$ Hydrogenation, *ChemNanoMat*, 2016, **2**(10), 989–996.

58 T. Wu, J. Lin, Y. Cheng, J. Tian, S. Wang, S. Xie, Y. Pei, S. Yan, M. Qiao, H. Xu and B. Zong, Porous Graphene-Confined Fe–K as Highly Efficient Catalyst for CO$_2$ Direct Hydrogenation to Light Olefins, *ACS Appl. Mater. Interfaces*, 2018, **10**(28), 23439–23443.